Flame Synthesis of Mixed Tin-Silver-Copper Nanopowders and Conductive Coatings

Munish K. Sharma, Di Qi, Raymond D. Buchner, and Mark T. Swihart
Dept. of Chemical and Biological Engineering, The University at Buffalo (SUNY), Buffalo, NY 14260

William J. Scharmach and Vasilis Papavassiliou
Praxair, Inc., Tonawanda, NY 14150

DOI 10.1002/aic.15132
Published online December 28, 2015 in Wiley Online Library (wileyonlinelibrary.com)

The single-step direct synthesis of tin-silver-copper nanopowders and nanostructured coatings using the flame-based high-temperature reducing jet (HTRJ) process is reported. Nanostructured coatings were deposited and sintered within the HTRJ reactor to study the effect of reductive sintering temperature on their electrical conductivity and surface morphology. Although the ultimate application of these nanoparticles is in printed electronics, which requires dispersing them as stable inks before depositing and sintering them, our approach of direct deposition from the gas phase provides an upper limit on the conductivity achievable with a given composition. The directly deposited coatings had high electrical conductivity, including a value of 2×10^6 S/m for 36 wt % Cu-40 wt % Ag-24 wt % Sn sintered at 200°C. This is twice the conductivity of a pure silver coating prepared under similar conditions. Moreover, similarly high electrical conductivity was achieved using only 20% Ag with sintering at 300°C. *AIChE J*, 62: 408–414, 2016
Keywords: tin-silver-copper, electrical conductivity, nanopowder, coatings

Introduction

Sn-Ag-Cu (SAC) alloys are used in solder applications, printed circuit boards, and dental fillings.[1–6] Historically, 63%Sn-37%Pb alloy was extensively used in the microelectronics industry.[1,4,7] However, due to the toxicity and environmental impacts of lead, the US and EU countries have banned lead-containing solders.[3,8,9] This created an urgent need for lead-free solders, which led to the development of nanosolders. Attributes of an ideal nanosolder alloy include low soldering temperature, absence of creep and fatigue due to thermal stresses, moderate surface tension, high electrical conductivity, and corrosion resistance.[3,10–13] Solder joints made with 96%Sn-3.5%Ag-0.5%Cu exhibit better electrical conductivity and mechanical strength compared with 63%Sn-37%Pb joints.[14] An emerging application of nanoscale SAC alloys is in metal-based conductive inks (CIs) for printable electronics.[3,15–19] These applications currently rely mainly on pure silver nanoparticle-based inks, but inks based on lower cost materials are of great interest. This need for lower-cost metal nanoparticle based CIs provide the primary motivation for this study.

Common phases reported in the SAC system include intermetallic compounds Cu_6Sn_5, Cu_3Sn, and Ag_3Sn.[20–23] Most prior research on this system has focused on compositions with a high Sn content (>95 wt %) to produce solders with melting points lower than that of pure Sn.[22] However, these high tin compositions are not ideal for CI applications in which properties closer to those of pure silver are desired. A key difference is that in printed electronics, the metal nanoparticles are not required to fully melt, as in soldering, but are only required to sinter sufficiently to create conductive paths. Over the past decade, researchers have mostly focused on the Sn-rich corner of the ternary Cu-Ag-Sn phase diagram, circled in red in Figure 1. Lin et al. produced 96.5%Sn-3.5%Ag using a process in which dry Ag and Sn powders were heated in a vacuum furnace and mixed and centrifuged with paraffin and dry ice.[8] Yung et al. prepared 96.5%Sn-3.0%Ag-0.5%Cu nanosolder alloys via a chemical reduction method using polyvinylpyrrolidone (PVP) and $NaBH_4$.[12] They identified SnO and SnO_2 phases, demonstrating that the surface of the nanosolders was oxidized. This oxide was later reduced by citric acid. The Cu_6Sn_5 phase was not detected by X-ray diffraction (XRD), probably due to the low Cu content. Bao et al. synthesized 99%Sn-1.0%Ag, 96.5%Sn-3.5%Ag, and 93.5%Sn-6.5%Ag nanosolders via an arc discharge process.[11] Jiang et al. produced SnAg nanosolders by a chemical reduction method and studied their thermal and wetting properties for solder melting point depression.[23] They observed the formation of Ag_3Sn along with Sn, and showed that the melting point of Sn depends nonlinearly on the nanoparticle size. Zou et al. fabricated 96.5%Sn-3.0%Ag-0.5%Cu nanoparticles less than 100 nm in diameter using a chemical reduction approach with $NaBH_4$.[3]

Additional Supporting Information may be found in the online version of this article.

Correspondence concerning this article should be addressed to M. T. Swihart at swihart@buffalo.edu.

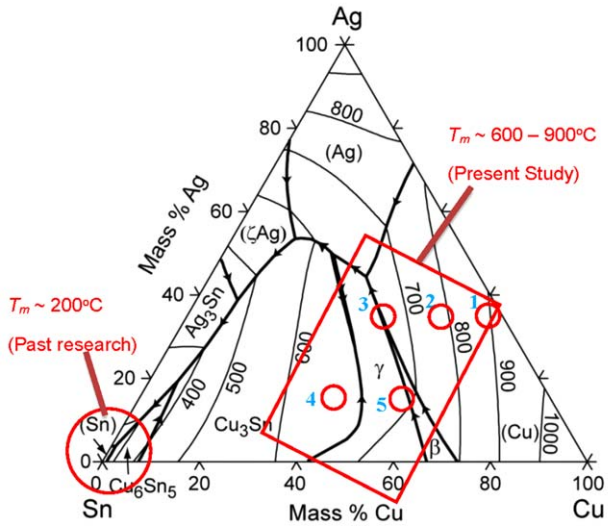

Figure 1. Ternary Cu-Ag-Sn phase diagram.

The larger red circle shows the focus of most prior research, which was aimed at producing lead-free solder materials. The red rectangle and smaller red circles indicate the range of compositions explored in the present study. Compositions of positions within the rectangle are: (position 1: 40 Ag-58 Cu-2 Sn; position 2: 40 Ag-50 Cu-10 Sn; position 3: 40 Ag-36 Cu-24 Sn; position 4: 20 Ag-50 Cu-30 Sn; position 5: 20 Ag-36 Cu-44 Sn). Adapted from www.metallurgy.nist.gov. [Color figure can be viewed in the online issue, which is available at wileyonlinelibrary.com.]

Reviewing the above studies, we see that chemical reduction is a relatively inexpensive and convenient method of preparing nanosolder alloys, particularly at laboratory scale, but has some limitations, including incomplete precursor utilization and challenges in controlling composition of complex alloys. High energy milling and arc discharge methods are energy intensive and have relatively high operating costs. Flame-based aerosol synthesis can provide a continuous, scalable, one step approach to produce nanoparticles and nanoparticle-based coatings. Numerous researchers have prepared metal and metal oxide nanoparticles via aerosol methods, as described in several reviews.[24–28] However, few studies have reported aerosol synthesis of materials in the SAC system. In earlier work, we demonstrated continuous one-step synthesis of bimetallic copper-nickel[29] and copper-silver[30] nanostructured coatings by deposition and sintering of nanoparticles produced as an aerosol using the flame driven high temperature reducing jet (HTRJ) process. Blattmann et al. used flame aerosol deposition of silver nanoparticles onto bare or polymer-coated glass substrates followed by polymer spin-coating to produce flexible, free-standing conductive films.[31] Starsich et al. used reducing flame-spray pyrolysis to produce cobalt nanoparticles and incorporate them into a magnetic metal-polymer nanocomposite.[32]

The composition range considered in this study is indicated by a red rectangle on the ternary phase diagram shown in Figure 1.[33] The goal of this study was to synthesize and characterize SAC nanoparticles and nanostructured films of varying composition using the HTRJ process developed by Scharmach et al.[34]The compositions studied here were selected as follows. In our previous study on the Cu-Ag bimetallic system, we found an optimum coating with composition 58 wt % Cu-42 wt % Ag.[30] We replaced 2 wt % Ag with Sn which corresponds to position 1 in Figure 1 to investigate the effect of a small addition of Sn on conductivity and surface microstructure. We then moved horizontally on the phase diagram (keeping Ag wt % fixed at 40 wt %, positions 1, 2, and 3) while replacing copper with tin. This was done in an effort to reduce sintering temperature of coatings and thereby increase conductivity at fixed Ag content. Finally, we moved vertically down on the phase diagram, reducing silver content to bring the overall cost of coatings down (position 4 and 5). Although the CuAgSn phase diagram is for bulk systems, it can reasonably be used to predict the possible phases that will form in nanomaterials. Certainly metastable materials can be produced by processes like those used here, but the bulk phase diagram nonetheless provides guidance with respect to the phases likely to be observed.

Experimental Section

Materials and synthesis

Water soluble nitrate and sulfate metal precursors used in these experiments included silver nitrate (ACS reagent, ≥99.0%, Acros Organics), copper nitrate (ACS reagent, ≥98.0%, Acros Organics), and tin sulfate (97%, Acros Organics). The HTRJ reactor was described in detail by Scharmach et al.[34] Oxygen at a flow rate of ~2.3 standard liters per minute (SLM) flowing through a central inlet and a larger flow of hydrogen and nitrogen (~14 SLM total) flowing in a concentric annular region formed an inverted diffusion flame. Excess hydrogen was always used, so the flame temperature depended primarily on the oxygen flow rate. The products of combustion, comprised of unreacted hydrogen, water vapor, and nitrogen, were accelerated through a converging-diverging nozzle. The liquid precursor mixture was delivered within the nozzle by four small symmetrically arranged inlets using a syringe pump at a total flow rate of 180 mL/h. The high-velocity gaseous stream atomizes the precursor solution, which rapidly evaporates and decomposes, producing metal or metal oxide particles. This reactor provides a general method of producing nanoparticles of metals that can be reduced by H_2 in the presence of water. To arrest particle growth, a varying flow rate of cold nitrogen gas was used in the quench section downstream of particle formation chamber. Nanoparticles were thermophoretically deposited on 12.5 mm diameter glass windows (Edmund Optics) to produce sintered coatings. The glass substrate was mounted perpendicular to the gas flow, on the reactor axis, just above the reactor exit. The temperature of the substrate was measured during the deposition process using a k-type thermocouple (Omega). The substrate temperature was controlled by varying the flow rate of cold nitrogen gas. A flow rate of 100 SLM was used to maintain the substrate temperature at ~200°C. Flows of 65 SLM and 50 SLM yielded substrate temperatures of ~300°C and 400°C, respectively. For all experiments reported here, the precursor solution had a total metal concentration of 10 mM. Nanoparticles were collected using a 293 mm diameter Durapore brand polyvinylidene difluoride (PVDF) membrane filter with 0.22 micron pore size (Millipore). This provides efficient particle collection with minimal pressure drop at the flow rates used in this study. Only a small fraction of the product nanoparticles were deposited on the glass substrate. Most were collected on the filter. The nanoparticle deposition time per batch was ~3 h. The sintering time is the same, because the particles are

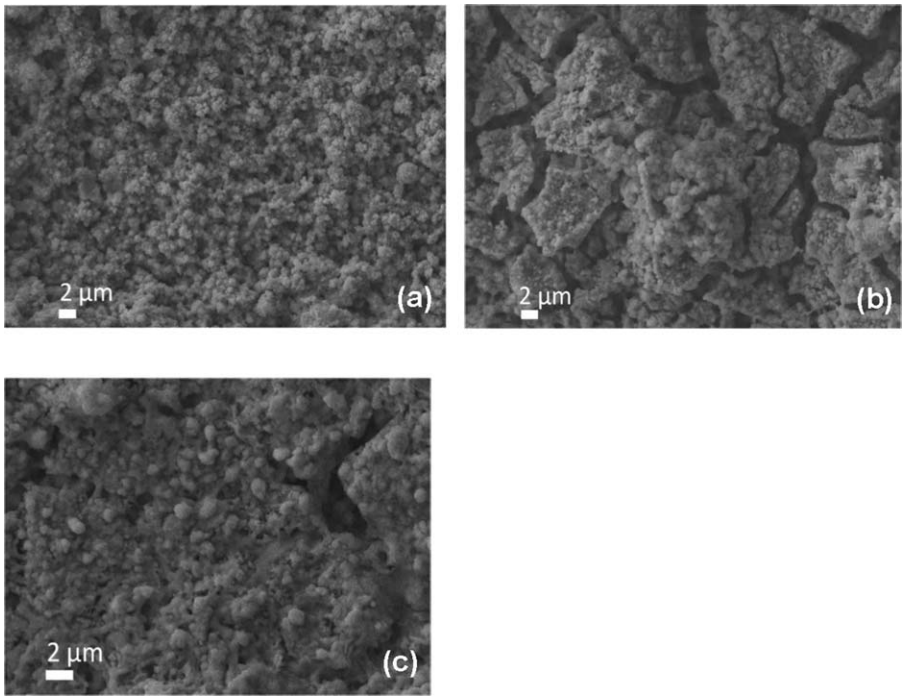

Figure 2. Scanning electron micrographs (SEM) of 40 Ag-36 Cu-24 Sn nanostructured coatings sintered at (a) 200°C, (b) 300°C, and (c) 400°C.

produced and deposited simultaneously. The average coating thickness was in the range of 1–5 μm.

Nanoparticle characterization

The nanopowders and nanostructured coatings were analyzed by a series of methods: XRD (Rigaku Ultima IV X-Ray diffractometer), transmission electron microscopy (TEM) (JEOL JEM 2010 at an accelerating voltage of 200 KV), and scanning electron microscopy (AURIGA™ CrossBeam® Workstation (FIB-SEM) from Carl Zeiss SMT) with an Oxford Instruments X-Max® 20 mm^2 energy dispersive X-ray spectroscopy (EDS) detector and INCA® software for elemental composition determination. A custom-built electrostatic sampler, similar to that described by Dixkens and Fissan[35] was used for collecting particles directly onto TEM grids for offline analysis. For bulk electrical conductivity of coatings, a four-point probe with a Keithley 2400 sourcemeter was used.

Results and Discussion

Scanning electron microscopy and EDS characterization—(Cu 36 wt %-Ag 40 wt %-Sn 24 wt% coating)

The motivation behind choosing this composition was to see the effect of moving from right to left in the ternary phase diagram, starting from a Cu-Ag combination shown in our previous work to be near the minimum Ag content required to produce conductive films.[30] This was done by decreasing Cu wt % at fixed Ag wt % and increasing Sn wt %. Addition of tin resulted in formation of the Ag-Sn intermetallic compound Ag_3Sn. The electrical conductivity of films at this composition reached 10^6 S/m. This conductivity is one order of magnitude lower than that of bulk Sn (8.69×10^6 S/m at 273 K)[36] and exceeds requirements for metal nanoparticle based CI formulations.[37–40]

Effect of reductive sintering (under H_2) on microstructure of coatings

The nanostructured coatings were sintered at 200°C, 300°C, or 400°C under the reducing H_2 atmosphere present in the HTRJ reactor, where the postcombustion gases consist of H_2, H_2O, and N_2. Figure 2 shows the effect of reductive annealing. Figure 2a shows the coating sintered at 200°C, which was found to be porous. After annealing at 300°C, the coating started cracking, as shown in Figure 2b, causing a decrease in conductivity by one order of magnitude, as discussed further below. Figure 2c shows the coating sintered at 400°C. Sintering at this temperature led to formation of the intermetallic copper-tin compound Cu_3Sn, as shown by XRD. The electrical conductivity increased to 10^6 S/m after sintering at 400°C.

Energy dispersive X-ray spectroscopy (EDX) elemental mapping was used to characterize the mixing of the three elements, as seen in Figure 3, which presents the distribution of Cu, Ag, and Sn in the nanostructured coatings sintered at 200°C and 400°C. Figure 3a shows a scanning electron microscopy (SEM) image of a film sintered at 200°C, and Figure 3b is the EDX elemental map showing the distribution of Cu, Ag, and Sn corresponding to Figure 3a. Figures 3c, d shows the same analysis for a film sintered at 400°C. In films sintered at 200°C, all three elements were well mixed, but at higher sintering temperature (400°C), we observed formation of segregated Ag-rich and Sn-rich domains. This suggests that the thermophoretically-deposited nanoparticulate film is metastable, and evolves toward a thermodynamically more stable phase-segregated state on annealing at sufficiently high temperature. The EDX spectrum of a 40 Ag-36 Cu-24 Sn (numbers indicate wt %) coating sintered at 200°C is provided in the Supporting Information. The ratio of the metals in the coating is consistent with that in the precursor mixture. This illustrates the ability of the HTRJ process to control

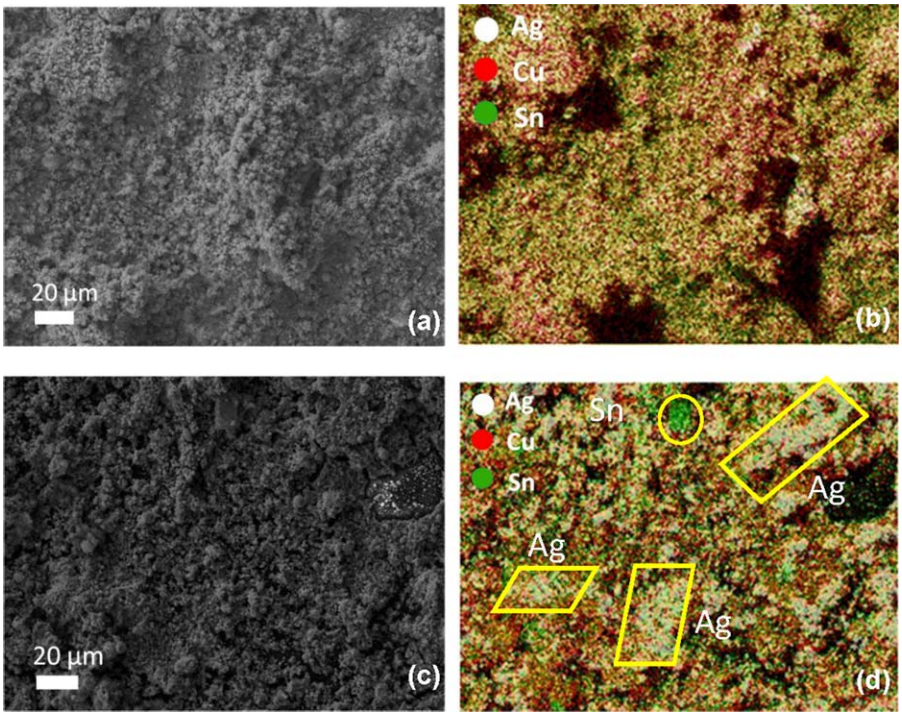

Figure 3. SEM images ([a] and [c]) and EDX based composition maps ([b] and [d]) of sintered 40 Ag-36 Cu-24 Sn nanostructured coatings; (a) and (b) show a film sintered at 200°C; (c) and (d) show a film sintered at 400°C.

[Color figure can be viewed in the online issue, which is available at wileyonlinelibrary.com.]

composition via complete conversion of precursors to product particles.

In this study, we have not performed detailed analysis of the film and powder composition, based in our prior observations in other systems for which the film and powder composition matched the precursor composition almost exactly. In our study of Cu-Ni powders and films in the HTRJ system,[29] we performed extensive composition analysis of powders collected on filter paper and particulate films deposited on glass substrates, using both inductively coupled plasma optical emission spectroscopy (ICP-OES) and EDX. We found close agreement between the two techniques and also between the measured compositions and the nominal compositions based on precursor composition. Similarly, in our previous study of Cu-Ag nanoparticles and films,[30] we observed close agreement between EDX-based composition analysis and the nominal composition based on precursor composition. The consistency of the results in this study (EDX-based composition in good agreement with nominal composition, similar nanoparticles observed in TEM) with those previous studies provides confidence that the product films consist of partially sintered nanoparticles of approximately the same composition as the nominal precursor composition. The morphology of particles obtained from the HTRJ process is irregular and non-spherical as seen in our earlier published studies.[29,30] The morphology of particles of four different compositions are shown in Supporting Information Figure S1. No dramatic changes in morphology with composition are observed.

Powder X-Ray diffraction studies

Powder XRD measurements were made on nanopowders collected on filter paper and on coatings deposited on glass substrates. The effect of sintering on the phase evolution was elucidated via XRD. Figure 4 compares X-Ray diffraction patterns from the 40 Ag-36 Cu-24 Sn nanopowder, the corresponding coating sintered at 200°C, and the coating sintered at 400°C. The crystallographic phases, with their respective Miller indices (hkl), corresponding to each peak position are shown in Figure 4. As is typical of XRD patterns of particles in this size range, particularly in thin films, the peaks are significantly broadened and the noise level precludes identification of the weakest reflections from each phase. Thus,

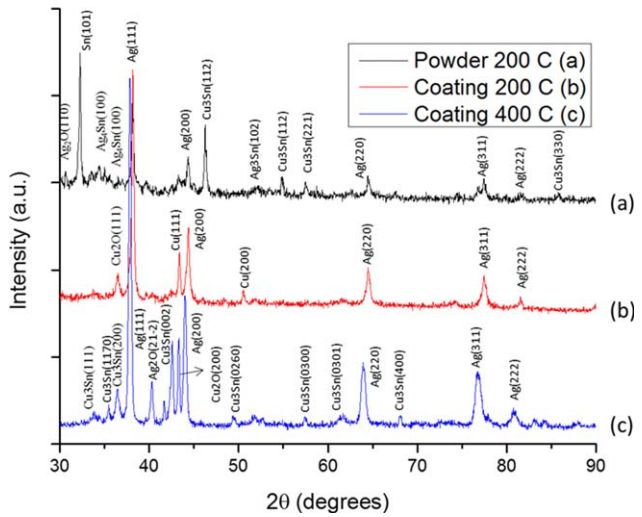

Figure 4. X-Ray diffraction patterns of 40 Ag-36 Cu-24 Sn powder, and nanostructured coatings sintered at 200°C and 400°C.

[Color figure can be viewed in the online issue, which is available at wileyonlinelibrary.com.]

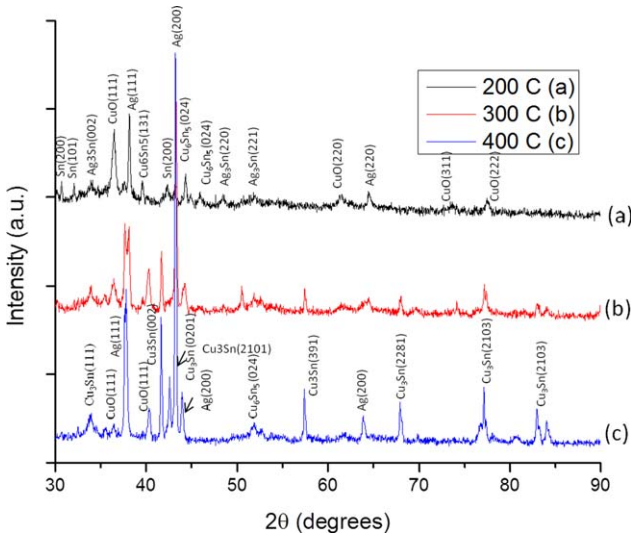

Figure 5. X-Ray diffraction patterns of 20 Ag-50 Cu-30 Sn nanostructured coatings sintered at 200°C, 300°C, and 400°C.

[Color figure can be viewed in the online issue, which is available at wileyonlinelibrary.com.]

quantitative fitting, by Reitveld refinement, did not produce unique or meaningful results for the phase fractions and crystallite sizes, and there is some ambiguity in some of the assignments of overlapping peaks. The XRD pattern of the powder shows the presence of a pure Sn phase, which is not seen in the films. This phase is evident from the peak at 2 $\theta = 32.25°$ corresponding to the Sn (101) plane. Peaks assigned to intermetallic compounds of Sn with Cu and Ag (e.g., Cu_3Sn and Ag_3Sn) are also present in powder XRD patterns. The coating sintered at 400°C consists mostly of Cu_3Sn and Ag phases. These observations suggest that tin particles form separately from the other materials, but that tin diffuses into the other metals during sintering at 200°C. At higher sintering temperature (400°C) Ag segregates from the other metals, as also suggested by the SEM and EDX results. Some of the copper is present as oxides. We are confident that within the reactor, the particles are in their metallic form. The thermodynamics of hydrogen reduction of Ag and Cu in the presence of water are very favorable. The reactor is a closed (vacuum/pressure tight) system, so no entrainment of air is possible. These nanostructured materials are simply subject to surface oxidation upon exposure to the ambient environment.

Figure 5 shows the powder XRD patterns for another composition, 20 Ag-50 Cu-30 Sn, indicated by circle 5 in the ternary phase diagram shown in Figure 1. This composition corresponds to the γ-phase region below the phase boundary. This composition was chosen to see the effect of lowering Ag wt % on the electrical conductivity. In this case, the coating sintered at 200°C shows the presence of some pure Sn, as shown by peaks Sn(200), Sn(101), and $Ag_3Sn(002)$ in the XRD pattern. The crystallographic phases with their Miller indices (hkl), corresponding to each peak position are shown in Figure 5. This phase was not present in coatings sintered at 300°C and 400°C. Some copper in the film sintered at 200°C was oxidized, as shown by peaks CuO(311)and CuO(222). Coatings sintered at 300°C and 400°C contained more intermetallic phases. For example, peaks of $Cu_3Sn(002)$ and $Cu_3Sn(391)$ in the coating sintered at 400°C show the presence of Cu_3Sn, which is also evident in the coating sintered at 300°C, but not in the coating sintered at 200°C. We believe that separate Sn nanoparticles are formed in the gas phase. In the nanoparticles deposited on the glass substrate and sintered at 200°C or higher, the Sn diffuses into the other nanoparticles and the pure Sn phase disappears. However, for particles collected on the filter, which is at much lower temperature, this does not occur and the Sn phase remains present.

As noted above, several of the XRD patterns in Figures 4 and 5 show the presence of a significant amount of oxides. While the presence of Ag_2O is generally tolerable in CI applications, because of its relatively high conductivity, the presence of CuO, Cu_2O, and mixed oxides are undesirable. The conductivity results shown below clearly indicate that if films of these particles are sintered under reducing conditions, they remain conductive after exposure to air and the accompanying surface oxidation. This may not be the case for particles that suffer surface oxidation prior to sintering. Thus, conducting inks prepared from these particles may have to be prepared

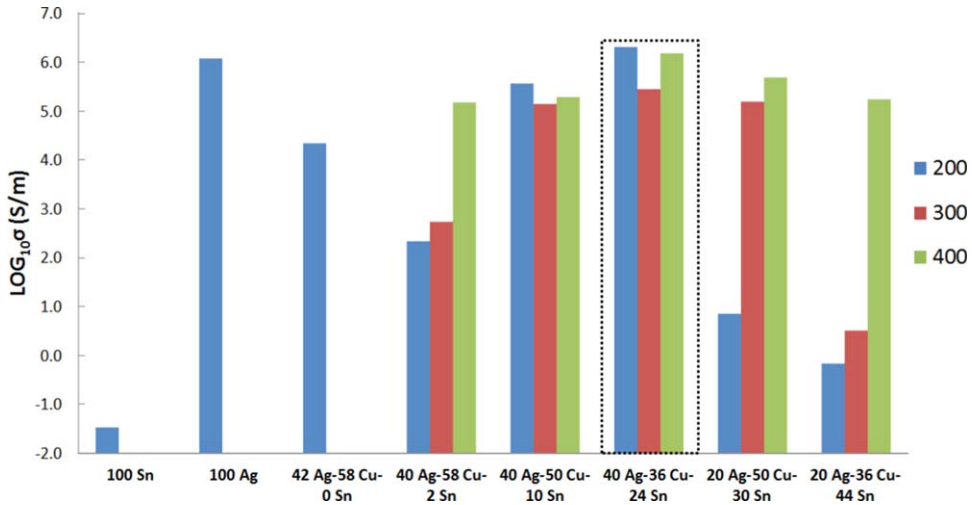

Figure 6. Semilog plot of electrical conductivity for the set of five points in the Cu-Ag-Sn phase diagram at three different sintering temperatures, 200°C, 300°C, and 400°C.

Results for pure silver, pure tin, and the 42Ag-58Cu film reported in our previous study[30] are included for comparison. [Color figure can be viewed in the online issue, which is available at wileyonlinelibrary.com.]

under an inert environment and incorporate ligands or dispersants that prevent oxidation. Sintering may still have to be performed in a reducing environment.

Note that in this study we have not produced ternary Cu-Ag-Sn alloy nanoparticles of uniform composition, even at overall compositions where ternary compounds are possible. Rather, we have produced an overall ternary mixture of copper, silver, and tin. This results in formation of some binary intermetallic compounds. The three elements are intimately mixed at the nanoparticle scale (length scales of a few tens of nm or more) but not at the atomic scale. As illustrated by the XRD patterns of Figures 4 and 5 the films and powders are a mixture of different metals and binary intermetallic compounds.

Electrical conductivity results—effect of reductive sintering temperature

The electrical conductivity was measured for the coatings corresponding to the five points in the ternary phase diagram shown in Figure 1. After sintering the coatings inside the reactor (under H_2), electrical conductivity measurements were done using a standard four-point probe method, in air. The conductivity was measured one day after deposition. The coating was stored in an inert atmosphere glove box prior to conductivity measurements. Figure 6 presents the electrical conductivity results, on a log scale. It compares conductivity values for compositions as indicated in Figure 1 (position 1: 40 Ag-58 Cu-2 Sn; position 2: 40 Ag-50 Cu-10 Sn; position 3: 40 Ag-36 Cu-24 Sn; position 4: 20 Ag-50 Cu-30 Sn; position 5: 20 Ag-36 Cu-44 Sn), along with pure silver, pure tin and a 58 Cu-42 Ag coating, each sintered at 200°C. The two major conclusions that can be drawn from this analysis are: (1) electrical conductivity increases with increasing sintering temperature except for the 40 Ag-36 Cu-24Sn composition and 40 Ag-50Cu-10 Sn; (2) the Ag 40-36 Cu-24Sn film has an electrical conductivity of 1.98×10^6 S/m at 200°C sintering temperature, which is twice the value of electrical conductivity obtained for a 100% Ag coating prepared under the same conditions. Because the logarithmic scale of Figure 6 spans nine orders of magnitude, this factor of two differences is not obvious in the figure. Thus, the 40 Ag-36 Cu- 24 Sn composition is potentially well suited for preparing metal nanoparticle based inks due to its high electrical conductivity and low sintering temperature. The 20 Ag-50 Cu-30 Sn coating is also notable, because it provides very high conductivity at 300°C sintering temperature while using only 20 wt % silver.

Conclusion

In summary, we have synthesized Cu-Ag-Sn (SAC) nanoparticles and nanostructured coatings of various compositions using a prototype high-temperature reducing-jet reactor system. The synthesis involved use of low cost and water soluble precursors. This study provides new insights into lower-cost metal nanoparticles for use in formulating inks for printable, flexible electronics. Detailed characterization of the coatings revealed that nanoscale mixing among Cu, Ag, and Sn is achieved at 200°C sintering temperature. The morphology and composition of the coatings were analyzed using SEM and EDS. Well-mixed domains of Cu, Ag, and Sn were found in the coatings. At higher Sn wt % in the Cu-Ag-Sn mixture, higher sintering temperatures favored formation of intermetallic compounds of Cu and Ag with Sn such as Cu_3Sn, Ag_3Sn, and Cu_6Sn_5, as demonstrated by XRD. XRD shows the presence of a pure Sn phase in the nanopowders, which was not generally present in films. The highest electrical conductivity of 1.98×10^6 S/m for sintering at 200°C was obtained for 40 Ag-36 Cu-24 Sn films, sintered at 200°C. This value is twice that of a pure Ag coating synthesized under similar conditions. The increased sintering, presumably due to melting point depression upon incorporation of tin, is responsible for this improved performance, despite the lower conductivity of Sn compared with Cu and Ag. These results provide valuable insights into the electrical conductivity of tin-silver-copper coatings sintered at temperatures relevant for printed electronics applications.

Acknowledgment

The authors gratefully acknowledge financial support from the U.S. National Science Foundation (GOALI grant CBET-0652042).

Literature Cited

1. Pan HJ, Lin CY, Chou JH, Mohanty US, Lee YG. A top-down approach of making Sn-3.5Ag nanosolder alloy by swirl method. *Mater Sci Appl*. 2011;2:1298–1301.
2. Sang X, Du K, Ye H. An ordered structure of Cu_3Sn in Cu-Sn alloy investigated by transmission electron microscopy. *J Alloys Compd*. 2009;469:129–136.
3. Zou C, Gao Y, Yang B, Zhai Q. Melting and solidification properties of the nanoparticles of Sn3.0Ag0.5Cu lead-free solder alloy. *Mater Charact*. 2010;61:474–480.
4. Sidhu RS, Deng X, Chawla N. Microstructure characterization and creep behavior of Pb-free Sn-rich solder alloys: Part II. Creep behavior of bulk solder and solder/copper joints. *Metall Mater Trans A*. 2008;39A:349–362.
5. Shih TI, Lin YC, Duh JG, Hsu T. Electrical characteristics for Sn-Ag-Cu solder bump with Ti/Ni/Cu under-bump metallization after temperature cycling tests. *J. Electron Mater*. 2006;35:1773–1780.
6. Nghiep DM, Chieu LT, Son NA, Baum H. A new dental powder from nanocrystalline melt-spun Ag-Sn-Cu alloy ribbons. *Adv Technol Mater Mater Process J*. 2003;5:74–79.
7. Gao F, Mukherjee S, Cui Q, Gu Z. Synthesis, Characterization, and Thermal Properties of Nanoscale Lead-Free Solders on Multisegmented Metal Nanowires. *J Phys Chem C*. 2009;113:9546–9552.
8. Lin CY, Chou JH, Lee YG, Mohanty US. Preparation of Sn-3.5Ag nanosolder by supernatant process. *J Alloys Compd* 2009;470:328–331.
9. Nai SML, Wei J, Gupta M. Lead-free solder reinforced with multiwalled carbon nanotubes. *J Electron Mater*. 2006;35:1518–1522.
10. Sopousek J, Palcut M, Hodulova E, Janovec J. Thermal Analysis of the Sn-Ag-Cu-In Solder Alloy. *J. Electron Mater*. 2010;39:312–317.
11. Bao TT, Kim Y, Lee J, Lee J-G. Preparation and thermal analysis of Sn-Ag nano-solders. *Mater Trans*. 2010;51:2145–2149.
12. Yung KC, Law CMT, Lee CP, Cheung B, Yue TM. Size Control and Characterization of Sn-Ag-Cu Lead-Free Nanosolders by a Chemical Reduction Process. *J Electron Mater*. 2012;41:313–321.
13. Bozack MJ, Suhling JC, Zhang Y, Cai Z, Lall P. Influence of Surface Segregation on Wetting of Sn-Ag-Cu (SAC) Series and Pb-Containing Solder Alloys. *J Electron Mater*. 2011;40:2093–2104.
14. Liu B, Guo F. Electrical conductivity changes of bulk tin and Sn-3.0Ag-0.5Cu in bulk and in joints during isothermal aging. *Int J Miner Metall Mater*. 2010;17:453–458.
15. Bao N, Wang C, Zhu L, Song S. Effects of different solder alloys on reliability of 3D PLUS solder joint. *Adv Mater Res (Durnten-Zurich, Switz.)*. 2011;314–316:1038–1042.
16. Doan TQ, Boyle TJ, Ottley LAM, et al. Synthesis and characterization of nanoalloys for solder application. *Abstracts of Papers, 242nd ACS National Meeting & Exposition, Denver, CO*, 2011:CHED-212.
17. Hsiao L-Y, Duh J-G. Synthesis and characterization of lead-free solders with Sn-3.5Ag-xCu (x = 0.2, 0.5, 1.0) alloy nanoparticles by the chemical reduction method. *J Electrochem Soc*. 2005;152:J105–J109.
18. Kawashima I, Araki Y, Ohno H. Retardation of grain boundary reactions in silver-copper alloys by addition of tin. *Mater Trans JIM*. 1993;34:438–442.
19. Peng Y, Cullis T, Inkson BJ. Electrical nanowelding and bottom-up nano-construction together using nanoscale solder. *J Nanosci Nanotechnol*. 2010;10:7394–7397.

20. Wang D, Yuan Y, Luo L. Indium addition on intermetallic compound evolution in tin-silver solder bump. *Mater Trans*. 2011;52: 1522–1524.
21. Ray AKK, A. Ghosh, M. Microstructrual characterization of tin lead and lead free solder joint interface. In: *International Symposium on Advanced Materials and Processing, ISAMP-2007*. Bagalkot: Basaveshwar Engineering College, 2009.
22. Mishra R, Zemanova A, Kroupa A, Flandorfer H, Ipser H. Synthesis and characterization of Sn-rich Ni-Sb-Sn nanosolders. *J Alloys Compd*. 2012;513:224–229.
23. Jiang H, Moon K-s, Hua F, Wong CP. Synthesis and thermal and wetting properties of tin/silver alloy nanoparticles for low-melting point lead-free solders. *Chem Mater*. 2007;19:4482–4485.
24. Buesser B, Pratsinis SE. Design of Nanomaterial Synthesis by Aerosol Processes. In: Prausnitz JM, ed. *Annu Rev Chem Biomol Eng*. 2012;3:103–127.
25. Mueller R, Madler L, Pratsinis SE. Nanoparticle synthesis at high production rates by flame spray pyrolysis. *Chem Eng Sci*. 2003;58: 1969–1976.
26. Rosner DE. Flame synthesis of valuable nanoparticles: Recent progress/current needs in areas of rate laws, population dynamics, and characterization. *Ind Eng Chem Res*. 2005;44:6045–6055.
27. Swihart MT. Vapor-phase synthesis of nanoparticles. *Curr Opin Colloid Interface Sci*. 2003;8:127–133.
28. Teoh WY, Amal R, Madler L. Flame spray pyrolysis: An enabling technology for nanoparticles design and fabrication. *Nanoscale*. 2010;2:1324–1347.
29. Sharma MK, Qi D, Buchner RD, Scharmach WJ, Papavassiliou V, Swihart MT. Flame-driven Aerosol Synthesis of Copper–Nickel Nanopowders and Conductive Nanoparticle Films. *ACS Appl Mater Interface*. 2014;6:13542–13551.
30. Sharma MK, Buchner RD, Scharmach WJ, Papavassiliou V, Swihart MT. Creating Conductive Copper-Silver Bimetallic Nanostructured Coatings Using a High Temperature Reducing Jet Aerosol Reactor. *Aerosol Sci. Technol*. 2013;47:858–866.
31. Blattmann CO, Sotiriou GA, Pratsinis SE. Rapid synthesis of flexible conductive polymer nanocomposite films. *Nanotechnology*. 2015;26: 125601.
32. Starsich FHL, Hirt AM, Stark WJ, Grass RN. Gas-phase synthesis of magnetic metal/polymer nanocomposites. *Nanotechnology*. 2014;25: 505602.
33. Chawla N. Thermomechanical behavior of environmentally benign Pb-free solders. *Int Mater Rev*. 2009;54:368–384.
34. Scharmach WJ, Buchner RD, Papavassiliou V, Pacouloute P, Swihart MT. A high-temperature reducing jet reactor for flame-based metal nanoparticle production. *Aerosol Sci Technol*. 2010;44:1083–1088.
35. Dixkens J, Fissan H. Development of an electrostatic precipitator for off-line particle analysis. *Aerosol Sci Technol*. 1999;30:438–453.
36. Haynes WM. Electrical resistivity of pure metals. In: *CRC Handbook of Chemistry and Physics, 92 ed*. Boca Raton: CRC Press, 2011–2012:12–41.
37. Grouchko M, Kamyshny A, Mihailescu CF, Anghel DF, Magdassi S. Conductive Inks with a "Built-In" Mechanism That Enables Sintering at Room Temperature. *ACS Nano*. 2011;5:3354–3359.
38. Luechinger NA, Athanassiou EK, Stark WJ. Graphene-stabilized copper nanoparticles as an air-stable substitute for silver and gold in low-cost ink-jet printable electronics. *Nanotechnology*. 2008;19:445201.
39. Greer JR, Street RA. Thermal cure effects on electrical performance of nanoparticle silver inks. *Acta Mater*. 2007;55:6345–6349.
40. Kim C, Nogi M, Suganuma K, Yamato Y. Inkjet-Printed Lines with Well-Defined Morphologies and Low Electrical Resistance on Repellent Pore-Structured Polyimide Films. *ACS Appl Mater Interfaces*. 2012;4:2168–2173.

Manuscript received July 1, 2015, and revision received Nov. 15, 2015.